Dynamical Structure and Evolution of Stellar Systems

Ven, Glenn van de

Citation

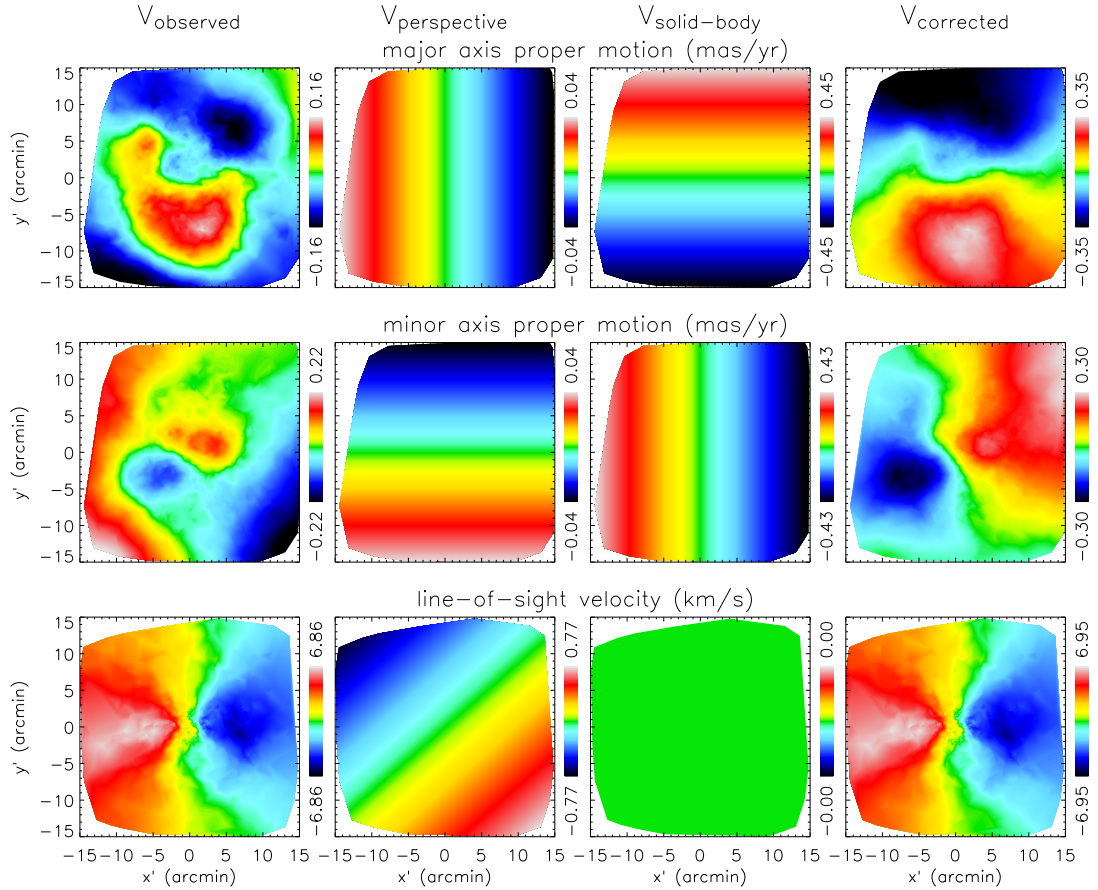Ven, G. van de. (2005, December 1). *Dynamical Structure and Evolution of Stellar Systems*. Retrieved from https://hdl.handle.net/1887/3740

APPENDIX: COLOR FIGURES

CHAPTER 2: FIGURE 6 — *The mean velocity fields of ω Cen corrected for perspective and solid-body rotation. The individual measurements are smoothed using adaptive kernel smoothening. From top to bottom: The mean ground-based proper motion in the major axis x'-direction and in the minor axis y'-direction, and the mean line-of-sight velocity. From left to right: Observed velocity fields of ω Cen, contribution from perspective rotation, contribution from solid-body rotation and the velocity fields after correcting for both. The perspective rotation is caused by the space motion of ω Cen. The solid-body rotation in the proper motions is due to relative rotation of the first and second epoch photographic plates by an amount of 0.029 mas yr^{-1} arcmin^{-1}.*
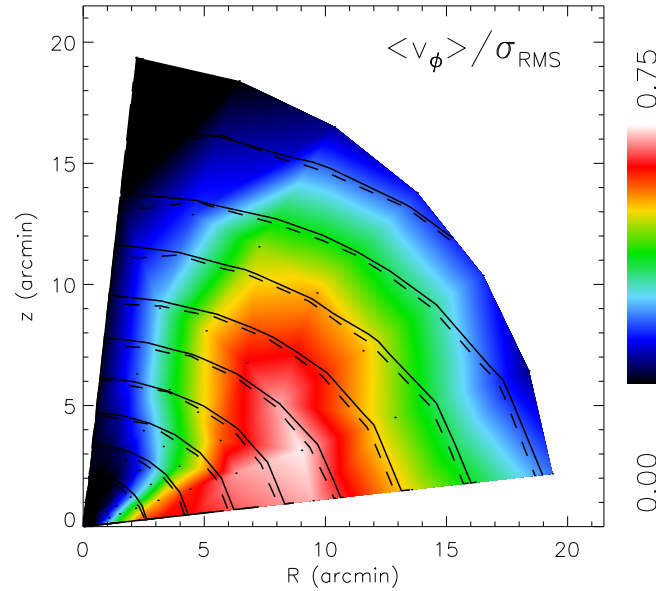
CHAPTER 2: FIGURE 17 — *The colors represent the mean azimuthal rotation $\langle v_\phi \rangle$ in the meridional plane as a function of equatorial plane radius R and height z, and normalized by σ_{RMS} (excluding the axes to avoid numerical problems). The black curves are contours of constant mass density, from the mass model (solid) and from the best-fit model (dashed), showing that the mass is well fitted.*
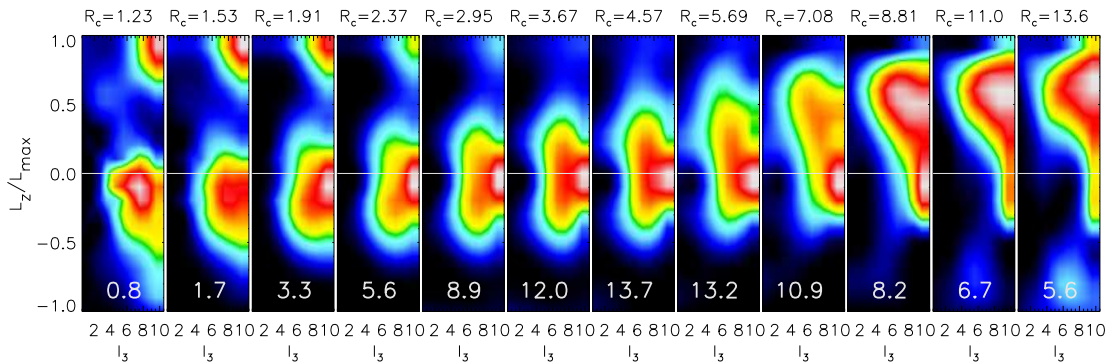

CHAPTER 2: FIGURE 19 — *The orbital weight distribution for our best-fit model of ω Cen. From left to right, the panels show the orbital weight distribution at increasing distance from the center, which corresponds to increasing energy. The radius R_c of the circular orbit at the corresponding energy is given above each panel. The radial range that is shown is constrained by the observations and contains more than 90% of the total cluster mass. The vertical axis represents the angular momentum L_z in units of L_{max}, the angular momentum of the circular orbit. The horizontal axis represents the third integral I_3, parameterized by the number of the (linearly sampled) starting angle of the orbit. Black shading corresponds to zero orbital weights, and white corresponds to the maximum orbital weight in each panel. At the bottom of each panel the fraction of the included mass with respect to the total mass is indicated (in %).*
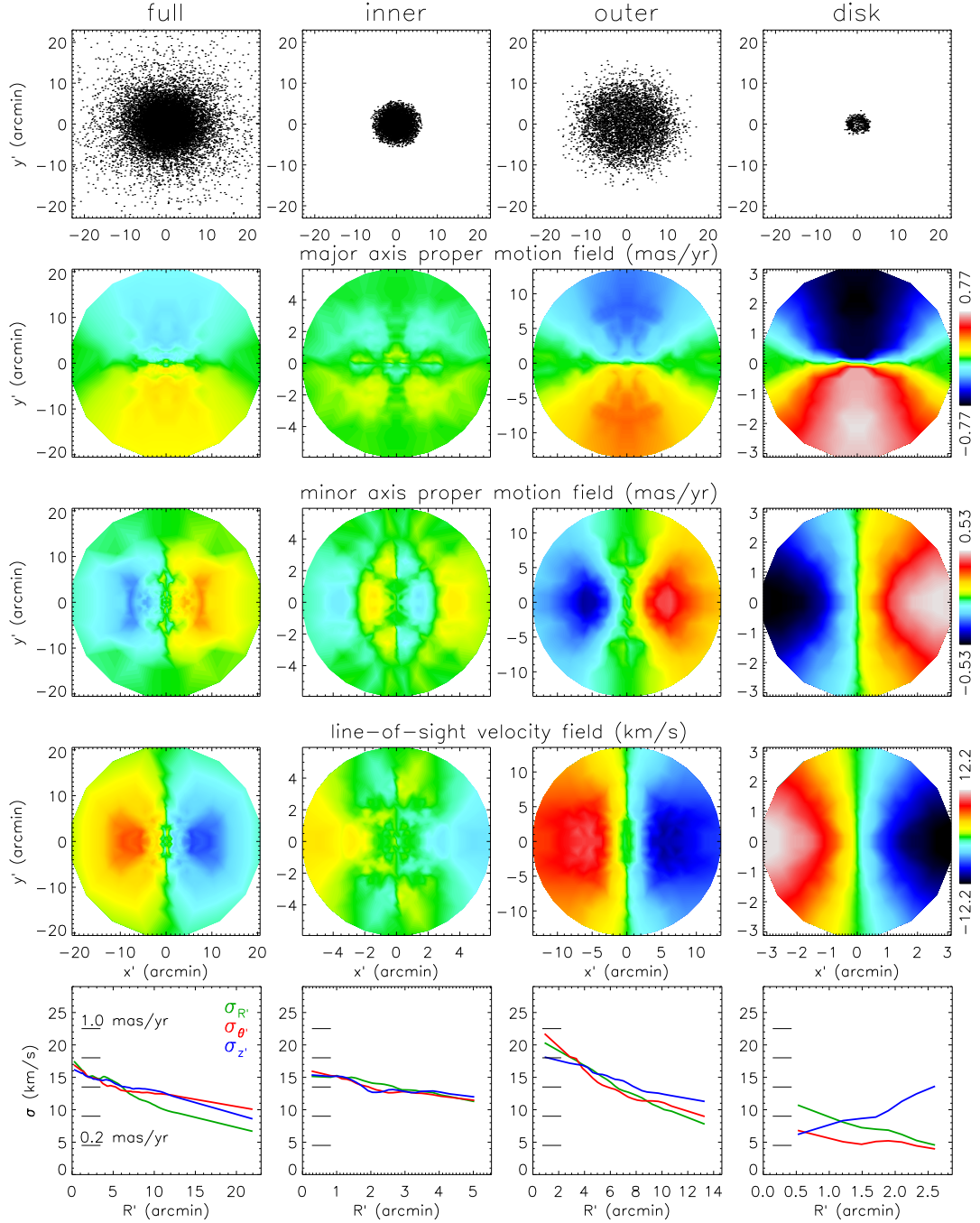
CHAPTER 2: FIGURE 20 — *Kinematics of different components in the distribution function of our best-fit model for ω Cen. From left to right: full distribution function, main inner component, main outer component and separate disk component between 1 and 3 arcmin (§ 9.4). From top to bottom: spatial distribution, mean velocity fields in the direction of the major x′-axis, the minor y′-axis and the line-of-sight z′-axis, and mean velocity dispersion profiles. The radial and tangential dispersion, $\sigma_{R'}$ (green) and $\sigma_{\theta'}$ (red), are on the plane of the sky and $\sigma_{z'}$ (blue) is the line-of-sight dispersion.*
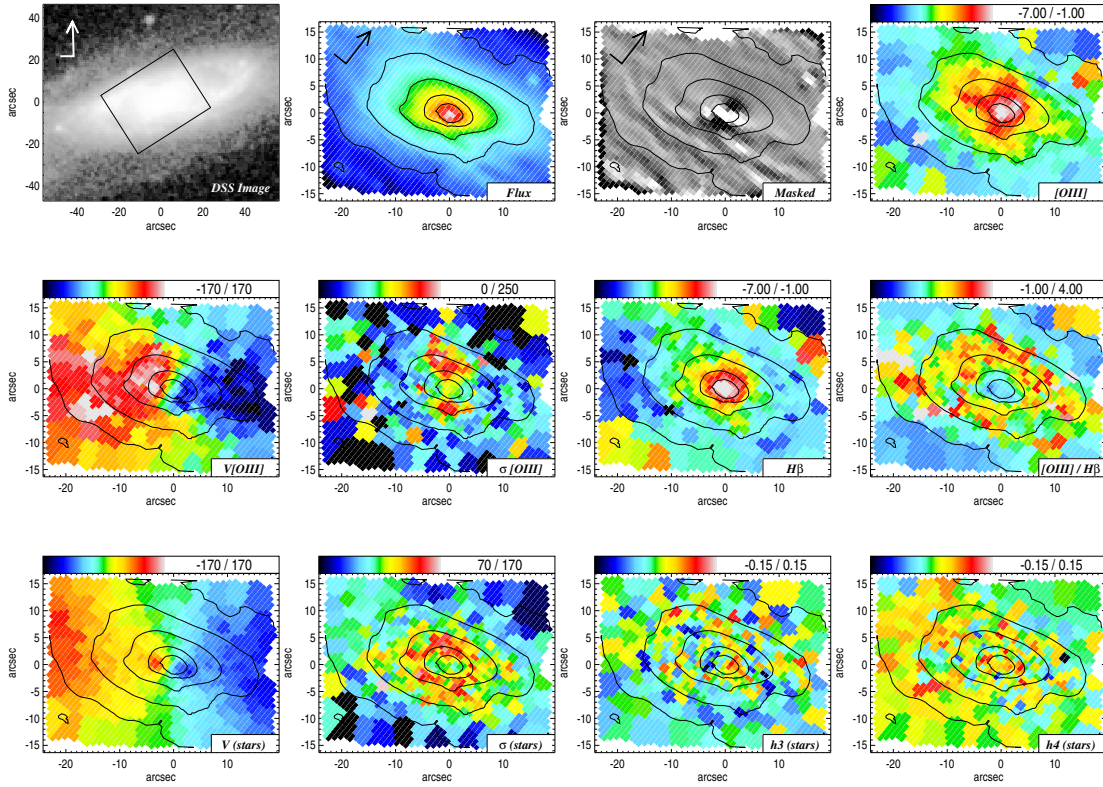
CHAPTER 3: FIGURE 1 — *Top Left: Digitized Sky Survey image of NGC 5448 with* SAURON *footprint and north-east orientation arrow. All other panels show the* SAURON *data. The stellar flux map and unsharp-masked* SAURON *image are given in mag arcsec^{-2} with arbitrary zero point, and north-east direction as indicated. The titles are indicated at the bottom right corner of each panel, and the plotting ranges are given at the top. All* SAURON *maps are overplotted with stellar contours in magnitude steps of 0.25, and all velocities and velocity dispersions are given in km s^{-1}.*
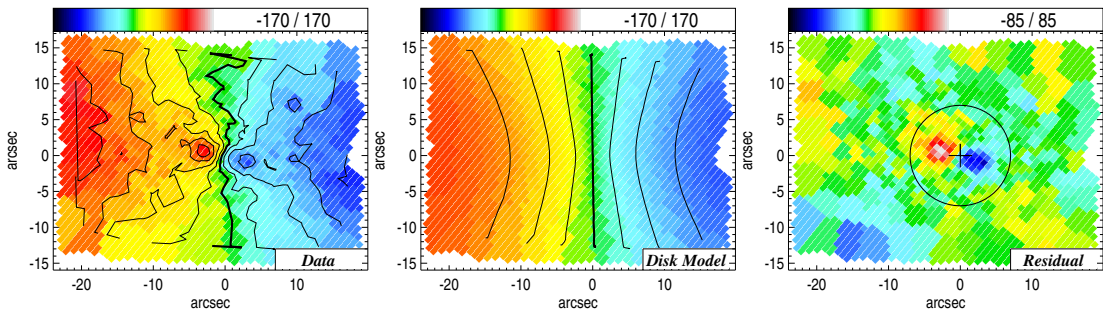

CHAPTER 3: FIGURE 3 — *A thin isothermal disk model for the stellar velocity field of NGC 5448. The circle marks the 7″ region within which we find a disk-like structure. The disk model, fitted to the field outside this region, implies for the outer disk a scale length of 18″, $V_{\rm sys}$= 2002 km s^{-1}, and PA= $91°$. The orientation of the maps is the same as in Fig. 1 of Chapter 3 (see above).*
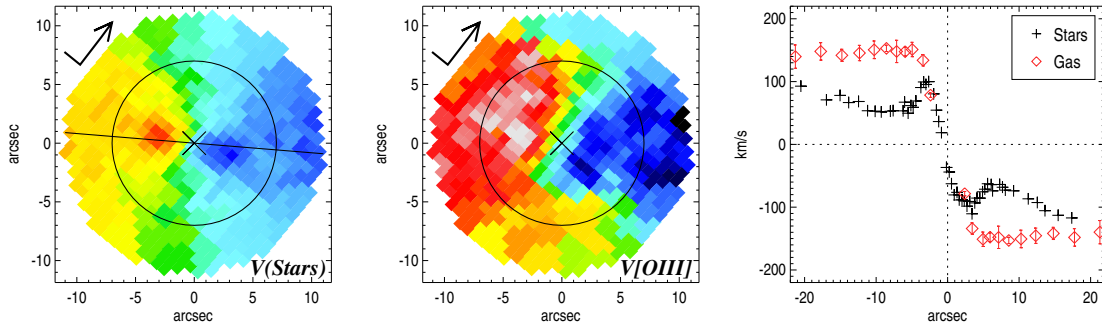
CHAPTER 3: FIGURE 5 — *Zooming into the central few arcseconds of the stellar and gaseous velocity maps of NGC 5448, using the same velocity range as in Fig. 1 of Chapter 3 (see above). Indicated are the north-east direction (arrow), the photometric PA (straight line) and the photometric center (cross). The over-plotted circle indicates the 7″ radius for comparison with Fig. 3 of Chapter 3 (see above). In the right panel, we present the stellar rotation curve (extracted along the photometric PA) together with the gas rotation curve derived from tilted-ring decomposition.*
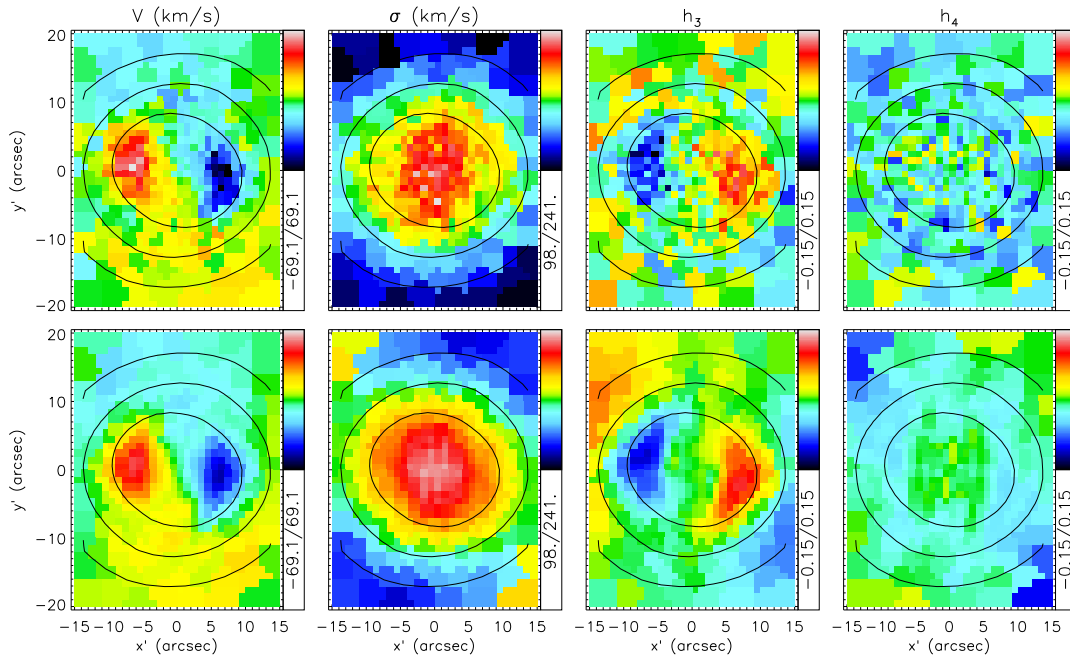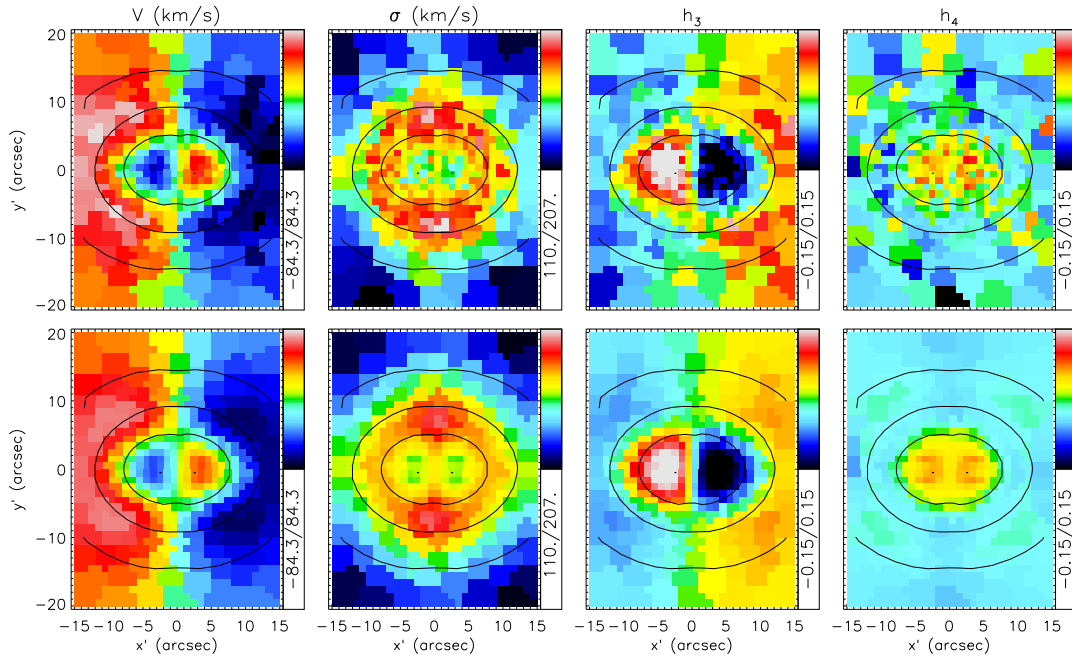

CHAPTER 4: FIGURE 6 — *Kinematic maps for a triaxial Abel model (top) and for the best-fit triaxial Schwarzschild model (bottom). From left to right: mean line-of-sight velocity V (in $km\,s^{-1}$), velocity dispersion σ (in $km\,s^{-1}$) and Gauss-Hermite moments h_3 and h_4. The line-of-sight kinematics of the input Abel model have been converted to observables with realistic measurement errors as described in the text of Chapter 4. Isophotes of the surface brightness of the Abel model are overplotted in each map. At the right side of each map, the (linear) scale of the corresponding kinematics is indicated by the color bar, and the limits are given below.*
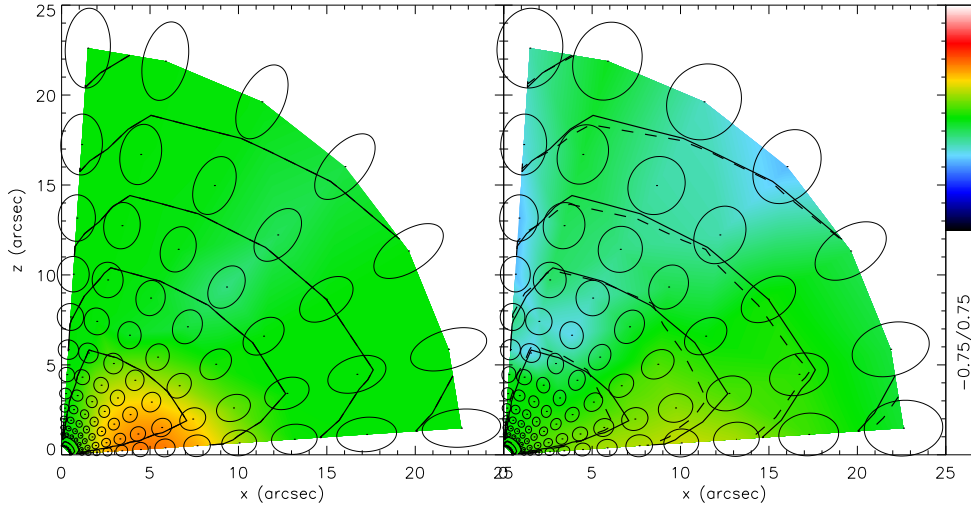
CHAPTER 4: FIGURE 9 — *The colors represent the mean motion $\langle v_y \rangle$ perpendicular to the (x,z)-plane, normalized by σ_{RMS} (excluding the axes to avoid numerical problems), for a triaxial Abel model (left) and for the best-fit triaxial Schwarzschild model (right). The ellipses are cross sections of the velocity ellipsoid with the (x,z)-plane. The black curves are contours of constant mass density in steps of one magnitude, for the input Abel model (solid) and for the fitted Schwarzschild model (dashed).*
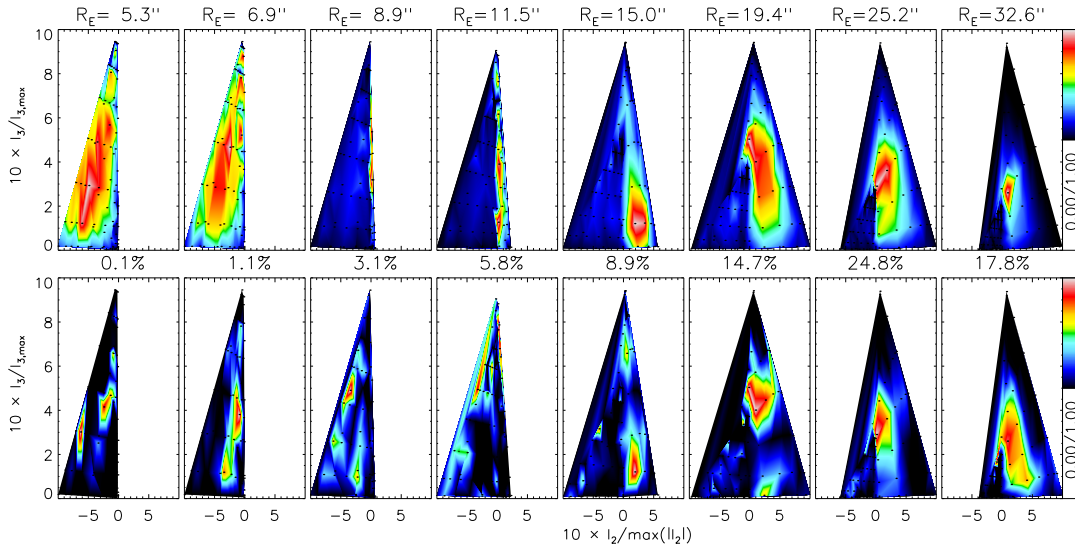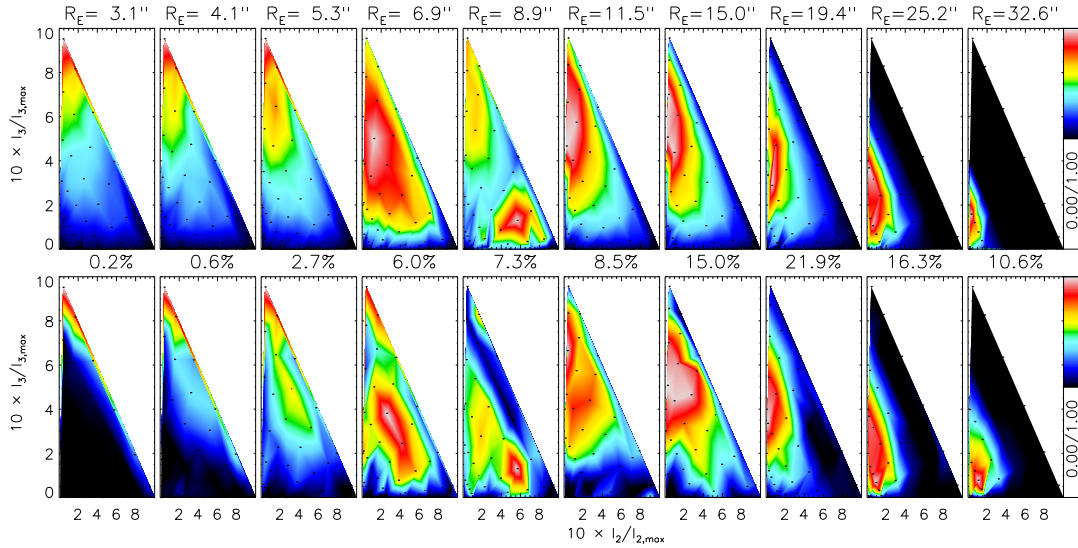

CHAPTER 4: FIGURE 11 — *The orbital mass weight distribution for the input triaxial Abel model (top) and for the fitted triaxial Schwarzschild model (bottom). From left to right the energy increases, corresponding to increasing distance from the center, indicated by the radius R_E (in arcsec) of the thin short-axis tube orbit on the x-axis. The vertical and horizontal axes represent respectively the second and third integral of motion, I_2 and I_3, normalized by their maximum amplitude (for given E). Between the two rows of panels, the fraction of the included mass with respect to the total mass is indicated (in %).*

CHAPTER 4: FIGURE 7 — *Kinematic maps for an oblate axisymmetric Abel model (top) and for the fitted axisymmetric Schwarzschild model (bottom), with parameters as in Fig. 6 of Chapter 4 above.*
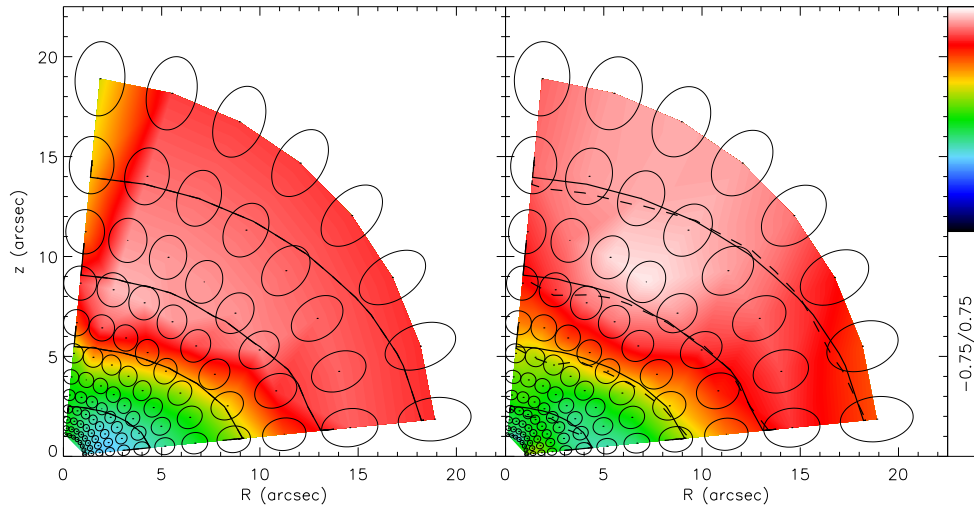
CHAPTER 4: FIGURE 13 — *The mean azimuthal motion $\langle v_\phi \rangle$ perpendicular to the meridional plane, normalized by σ_{RMS}, for an oblate axisymmetric Abel model (left) and for the best-fit axisymmetric Schwarzschild model (right), with parameters as in Fig. 9 of Chapter 4 above.*

CHAPTER 4: FIGURE 14 — *The mass weight distribution for an oblate axisymmetric Abel model (top) and for the fitted axisymmetric Schwarzschild model (bottom). Parameters are the same as in Fig. 4 of Chapter 4 above. In this case, the second integral of motion $I_2 = \frac{1}{2}L_z^2$, where L_z is the component of the angular momentum parallel to the symmetry z-axis.*
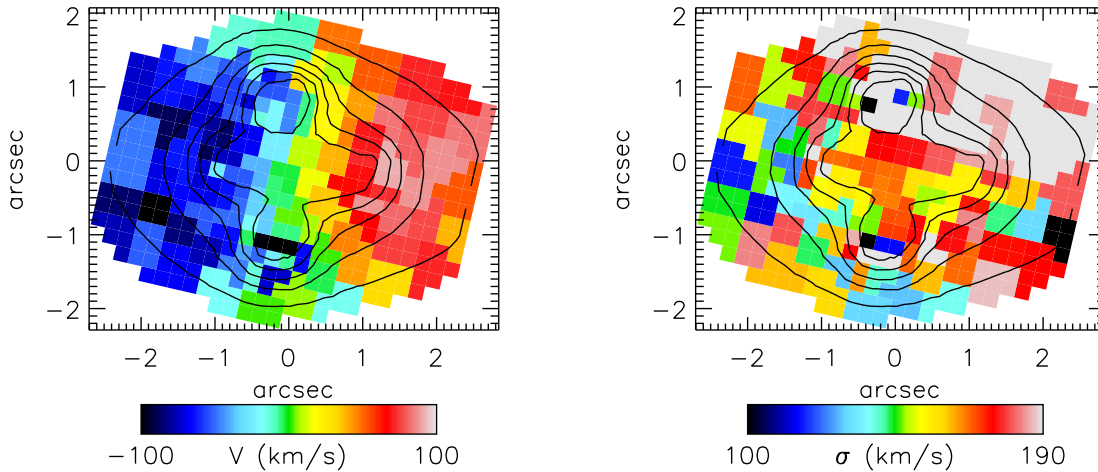
CHAPTER 6: FIGURE 4 — *Mean velocity and velocity dispersion field of the lens galaxy in the Einstein Cross as measured from observations with the integral-field spectrograph* GMOS *on Gemini-North. The overlayed contours of the reconstructed image show the positions of the quasar images, which affect the kinematics only very locally. The velocity field shows clear and regular rotation around the (vertically aligned) short-axis of the bulge. The velocity dispersion is fairly constant across the field, except for the region towards the upper-right, where systematic effects cause the dispersion to be overestimated.*